Two-stage Robust Reserve Coordinated Operation Based On Real-time Price Mechanism

Huiqiong Deng, Hui Wu*, Zhiwei Liang, Zhe Tong, and Junfu Shen

School of Electronic, Electrical Engineering and Physics, Fujian University of Technology, Fuzhou 350118, Fujian Province, China

** Corresponding author. E-mail: 2221905075@mail.fjut.edu.cn*

Received: Mar. 01, 2023; Accepted: Jun. 04, 2024

In order to cope with the impacts of uncertainty factors on the reliability and economy of system operation, a two-stage robust reserve optimization model is proposed to take into account the real-time price day-ahead and intraday. The proposed model consists of two phases: the first phase is the day-ahead decision-making phase, which improves the flexibility of grid operation by establishing a demand response model based on the load classification under real-time price; and the second phase is the intraday decision-making phase, which takes into account the uncertainty of the wind - photovoltaic power and the failure of the transmission line in order to improve the robustness of the grid in coping with the uncertainties. The day-ahead decision-making is a deterministic optimization problem, which is solved by a linear programming problem, while the intra-day decision-making is an adaptive robust optimization problem, which is solved by using the Strong Dyadic Theory (SDT) method. By combining the power data of wind and photovoltaic fluctuation intervals and load demand of a regional power grid, a simulation model is constructed to verify that the proposed robust model is effective in optimizing the reserve capacity of the system operation under multiple uncertainties, reducing the scheduling cost of the system in the worst scenario, and ensuring the safe and reliable operation of the system.

Keywords: Real-time price; Demand side response; Robust optimization; Coordinated operation; uncertainty

http://dx.doi.org/10.6180/jase.202505_28(5).0019

1. Introduction

With the proposal of the "dual-carbon" goal, the new power system, characterized by a high proportion of new energy penetration, is in the process of being laid out [1, 2]. The proportion of new energy sources, such as wind and solar, is also increasing, making the new power system, with values of security, flexibility, and greenness, an important direction for the transformation and upgrading of the traditional power system [3]. However, the problems caused by the randomness and intermittency of new energy output have been exacerbated with the increase in penetration rate, further aggravating the hazards of transmission line failures on the power system [4]. Therefore, the power system is in urgent need of more flexible and robust scheduling methods to reduce the risk of uncertainty factors.

Thermal power unit reserve and Demand Response (DR) represent effective measures for ensuring the stable operation of the power system. However, the increasing penetration of new energy sources, such as wind and solar, brings about escalating uncertainty in the availability of green energy. This growing uncertainty poses a challenge to the reliability of the reserve strategy. Consequently, experts from around the world have undertaken extensive research on optimizing unit reserve methods in response to this issue. One notable contribution is found in the literature [5], which proposes a two-stage optimal dispatch method for thermal power plants, addressing day-ahead and intraday considerations. This method takes into account both electric energy efficiency and the benefits of reserve opera-

tion. In a separate study, literature [6] introduces a reserve method specifically tailored for integrating new energy sources into the power system. This research analyzes the impact of reserve operation on grid scheduling, considering aspects such as grid security and new energy consumption. Another approach can be found in the literature [7], where a flexible reserve optimization model is established based on conditional value-at-risk. This model takes into consideration the constraints imposed by worst-case operational scenarios. Furthermore, literature [8] delves into the establishment of a wind-fire coordinated reserve method, analyzing its application in multi-state scenarios involving wind farms. Building upon the findings of these studies, our research aims to further advance the optimization of unit reserve strategies, addressing the challenges posed by the increasing uncertainty of new energy sources.

Demand-side response can be classified into two categories based on the response mechanism: Price-based Demand Response (PDR) and Incentive-based Demand Response (IDR). Incentive-based demand response stimulates users to participate in load shedding programs required by the system through economic compensation [9, 10]. On the other hand, price-based demand response guides users to adjust their electricity consumption based on price signals to achieve peak shaving and valley filling [11]. Research presented in literature [12] demonstrates that Real-Time Pricing (RTP) demand-side flexibility is adequate for balancing electricity supply and demand in real time, as well as achieving peak and valley adjustments. Literature [13, 14] explores the application of cloud energy storage systems (CES or CESS) in industrial users and renewable energy power plants to reduce the cost of energy storage systems and enhance their benefits in demand response and renewable energy generation through optimal allocation and cooperative game models. However, most existing studies consider the response of demand response power to electricity price as a simple linear relationship, neglecting the impact of nonlinear factors in the response model on the power system.

Modeling approaches for handling uncertainty in scenery and transmission line fault scenarios primarily consist of scenario-based stochastic optimization [15, 16] and robust optimization [17, 18]. Robust optimization has gained significant popularity among scholars worldwide due to its ability to address operational constraints of stochastic scenarios, enhance power system stability, and eliminate the need for scenario acquisition and extensive data processing. In reference [19], a method is proposed to identify high-risk links in transmission lines based on the similarity of current transfer. Additionally, literature [20] establishes a comprehensive outage fault set utilizing weighted current entropy and coupled branch median to examine transmission line vulnerability. Moreover, literature [21] incorporates power system line load factor metrics to reinforce grid robustness. However, most studies investigating the robustness of transmission line faults on the system solely rely on their respective proposed metrics. These studies often overlook the presence of other unknown factors and fail to consider the impact of line outages on grid dispatch operations under worst-case conditions.

In response to the limitations of current research, the paper proposes a comprehensive two-stage robust reserve optimization and coordinated operation method based on real-time price mechanism. This novel approach addresses the inadequacies by considering the impacts of scenery output uncertainty and transmission line fault shutdowns on the robustness of grid operations. Simultaneously, the research conducts co-optimization for thermal power unit reserve, price-based Demand Response (DR), and incentive-based DR under the real-time price mechanism. Furthermore, this paper compares the applicability of these two types of demand-side response under the real-time price mechanism.

2. Real-time price mechanism modeling

In the study of the management model based on PDR, the load response to price should be modeled, and PDR guides the customers to reasonably shift the time of use by adjusting the time-of-use price. In practice, the load $P_{\mathrm{L}}(t)$ under time-of-use prices are categorized into three types:

$$P_{\mathrm{L}}(t) = P_{\mathrm{L-I}}(t) + P_{\mathrm{L-II}}(t) + P_{\mathrm{L-III}}(t) \tag{1}$$

where: $P_{\mathrm{L-I}}(t)$ is Class I load; $P_{\mathrm{L-II}}(t)$ is Class II load; $P_{\mathrm{L-III}}(t)$ is Class III load.

Class I loads show a small response to price adjustments, and the demand-side response is not affected by real-time price, and their response loads are shown in Eq. (2):

$$P^{m}_{\mathrm{L-I}}(t) = P_{\mathrm{L-I}}(t) \tag{2}$$

Class II loads, which are characterized by energy-saving use of electricity or complementary substitution of electricity with other energy sources, are suitable for modeling the demand elasticity matrix of the power system. In this paper, the price elasticity coefficient n_{st} is used to portray the price adjustment situation in period t to reflect the load demand in period s. The demand elasticity matrix N is defined as well as the expression of the elements in the matrix as shown in Eq. (3). The load changes in setting

real-time prices are shown in Eq. (4), and its response load is shown in Eq. (5).

$$\begin{cases} N = (n_{st})_{T\times T} \\ n_{st} = \frac{\Delta P_L(s)/P_L(s)}{\Delta p(t)/p(t)} \end{cases} \tag{3}$$

where: $P_L(s)$ and $\Delta P_L(s)$ are the original load power of Class II loads and the response change power of time-share price in period s, respectively; $p(t)$ is the original time-share price level; the diagonal elements of N are the self-elasticity coefficients (the coefficients are positive), and the rest of the elements are the mutual-elasticity coefficients (the coefficients are negative).

$$\Delta P_{\mathrm{L-II}}(s) = \left(\sum_{t=1}^{n} e_{st}\Delta p(t)/p(t)\right) P_{\mathrm{L-II}}(s) \tag{4}$$

$$P^{m}_{\mathrm{L-II}}(t) = P_{\mathrm{L-II}}(t) + \Delta P_{\mathrm{L-II}}(t) \quad t \in 1,2,\cdots,T \tag{5}$$

Class III loads behave by consciously shifting that part of the load between periods and are suitable for load transfer rate modeling. In this paper, the number of periods with rising price m is denoted as $I = \{i_1, i_2, \cdots, i_m\}$, and the number of periods with falling price n is denoted as $J = \{j_1, j_2, \cdots, j_n\}$. Due to the implementation of rising real-time price at t_1, the load shifted during this period is allocated in J as shown in Eq. (6). Due to the implementation of decreasing real-time price at t_3, the period shifted load is allocated in I as shown in Eq. (7).

$$\begin{gathered} \Delta P_L(t_1,t_2) = \\ \frac{f[\Delta p(t_1)]\,|\Delta p(t_2)|\,P_L(t_1)}{\sum_{k\in J}|\Delta p(k)|} \\ t_1, t_4 \in I \end{gathered} \tag{6}$$

$$\begin{gathered} \Delta P_L(t_3,t_4) = \\ \frac{f[\Delta p(t_3)]\,|\Delta p(t_4)|\,P_L(t_3)}{\sum_{k\in I}|\Delta p(k)|} \\ t_3, t_4 \in J \end{gathered} \tag{7}$$

where: $\Delta p(t)$ denotes the difference between the implemented real-time price for period t and the original base price; $\Delta P_{\mathrm{L}}(i,j)$ denotes the amount of load transferred from period i to period j; and f is the load transfer rate function.

This paper refers to the load transfer rate model in literature, which is described as the relationship between the price change situation and the load transfer rate in each period, which is categorized into dead, linear and saturated zones, as shown in Eq. (8) and Appendix Figure A1.

$$f(\Delta p) = \begin{cases} 0, & 0 \le \Delta p \le a \\ K(\Delta p - a), & a \le \Delta p \le f_{\max}/K + a \\ f_{\max}, & \Delta p \ge f_{\max}/K + a \end{cases} \tag{8}$$

where: Δp is the absolute value of the price change; $f_{\max}$ is the maximum load transfer rate in the saturated zone; a is the dead zone value; $f_{\max}/K + a$ is the saturated zone inflection point; and K is the slope of the linear zone transfer rate curve.

Based on the implemented real-time price, the load response level under the real-time price mechanism can be obtained for Class III loads. When the implemented price for the period t is higher than the original time-sharing price, Eq. (9) is used. When the implemented price for period t is lower than the original time-sharing price, Eq. (10) is used for calculation.

$$P^{m}_{\mathrm{L-III}}(t) = P_{\mathrm{L-\ III}}(t) - \sum_{k\in J}\Delta P_{\mathrm{L-III}}(t,k) \quad t \in I \tag{9}$$

$$P^{m}_{\mathrm{L-\ III}}(t) = P_{\mathrm{L-\ III}}(t) + \sum_{k\in I}\Delta P_{\mathrm{L-\ III}}(t,k) \quad t \in J \tag{10}$$

Taken together, the response load $P^{\mathrm{PDR}}_{\mathrm{L}}(t)$ of the load decomposition-based PDR model is shown in Eq. (11):

$$P^{\mathrm{IDR}}_{\mathrm{L}}(t) = P^{m}_{\mathrm{L-II}}(t) + P^{m}_{\mathrm{L-III}}(t) \tag{11}$$

In this paper, the IDR model is added to the PDR model of real-time price mechanism, which is considered in a coordinated way in order to improve the efficiency of power system operation, as shown in Eq. (12):

$$P^{\mathrm{IDR}}_{\mathrm{L}}(t) = P^{m}_{\mathrm{L-II}}(t) + P^{m}_{\mathrm{L-III}}(t) \tag{12}$$

where: $P^{\mathrm{IDR}}_{\mathrm{L}}(t)$ is the IDR capacity at moment t.

3. Day-ahead - intraday robust optimization model

The joint operation system studied in this paper is shown in Appendix Figure A2, which mainly includes wind, photovoltaic, and thermal power, and the demand response types include both price-based and incentive-based. Deterministic dispatch is used in the day-ahead phase to minimize unit operating costs and reserve costs, and reserve capacity (unit reserve capacity and IDR reserve capacity) is reserved for stochastic scenarios that may occur in the intraday phase. The intraday phase calls spare capacity for uncertainty pools to ensure the safety of the operating system and looks for the worst risk scenarios, optimized to minimize the overall call cost. The day-ahead-intraday phases are coordinated to ensure stable and reliable system operation. The objective function of the model is shown in Eq. (13):

$$\min C_{\mathrm{main}} + \max_{U} \min C_{\mathrm{sub}} \tag{13}$$

where: C_{main} is the optimization objective for the day-ahead phase; C_{sub} is the optimization objective for the intraday phase; U is the uncertainty set, including the set of up and down fluctuations of the wind and photovoltaic plants and the set of failures of the power system lines.

3.1. Day-ahead phase optimization model

1. Objective function

$$\min C_{\text{main}} = \sum_{t=1}^{N_T}\sum_{g=1}^{N_G}\left(F_g\left(P_{g,t}^0\right) + C_g^{R+}R_{g,t}^{+} + C_g^{R-}R_{g,t}^{-}\right) + C_{Gi}^{U} + C_{Gi}^{D} + \sum_{t=1}^{N_T}\sum_{b=1}^{N_B} C_{b,t}^{\text{DDR}} P_{\text{L}}^{\text{IDR}} \tag{14}$$

where: N_G and N_B are the number of generators and buses, respectively; $P_{g,t}^0$ is the output of generator g at period t, 0 is denoted as the first-stage output power; F_g is the operating cost of the thermal unit; C_{Gi}^U and C_{Gi}^D are the startup and shutdown costs of the unit; $R_{g,t}^+$and $R_{g,t}^-$are the upward and downward reserve capacities of the unit; C_g^{R+} and C_g^{R-} are the reserve costs of the unit; $C_{b,t}^{\text{IDR}}$ is the reserve cost of the IDR.

2. Running costs of thermal power units

$$F_g\left(P_{g,t}^0\right) = \sum_{t=1}^{T}\beta\Delta t\left[a_g\left(P_{g,t}^0\right)^2 + b_g P_{g,t}^0 + c_g\right] \tag{15}$$

where: β is the coal price; a_g, b_g and c_g are the coal consumption coefficients of thermal power units.

In the modeling process, the nonlinear fuel cost function of thermal power units needs to be linearized in segments to accelerate the solution efficiency and improve the accuracy. Since there are large errors in the segment linearization analysis in the literature, this paper further improves the algorithm by subdividing the nonlinear fuel cost function of thermal power units into ω segments, as shown in Eqs. (16) and (17) and Appendix Figure A3.

$$F_g\left(P_{g,t}^0\right) = A_g i_{g,t} + \sum_{l=1}^{\infty} F_{l,g}\delta_l(g,t) \tag{16}$$

$$\begin{cases} \delta_1(g,t) \le T_{1,g} - P_g \\ \delta_2(g,t) \le T_{2,g} - T_{1,g} \\ \vdots \\ \delta_{\omega-1}(g,t) \le T_{\omega-2,g} - T_{\omega-1,g} \\ \delta_\omega(g,t) \le \bar{P}_g - T_{\omega-1,g} \end{cases} \tag{17}$$

where: $A_g = a_g + b_g P_g + c_g\left(P_g\right)^2$; $F_{l,g}$ is the cost of unit g in the segmental linearization curve in the l segment of the micro-increment; $\delta_l(g,t)$ is the power of unit g in the l segment at period t; $T_{l,g}$ is the upper limit of the power of unit g in the l segment; $i_{g,t}$ is a $0-1$ integer variable used to describe the state of the unit starting and stopping; $\bar{P}_g$ and P_g are the minimum and maximum output power of unit g, respectively.

3. Minimum start/stop time constraint for the unit

$$\begin{cases} \left(i_{g,t-1} - i_{g,t}\right)\left(T_{g,t-1} - T_{g,on}\right) \ge 0 \\ \left(i_{g,t} - i_{g,t-1}\right)\left(-T_{g,t-1} - T_{g,off}\right) \ge 0 \end{cases} \tag{18}$$

where: $T_{g,on}$ and $T_{g,\text{ off}}$ are the minimum periods of continuous start-up and shutdown of the unit, respectively.

4. Power balance constraints

$$\begin{aligned} &\sum_{g\in G_b} P_{g,t}^0 + \sum_{w\in W_b} P_{w,t}^0 + \sum_{v\in V_b} P_{v,t}^0 - L_{b,t} \\ &- \Delta P_{\text{L}}^{\text{PDR}} + \Delta P_{\text{L}}^{0,1\text{DR}} \\ &= \sum_{l:O_2(l)=b} P_{l,t}^0 - \sum_{l:Q_1(l)=b} P_{l,t}^0 \end{aligned} \tag{19}$$

where: G_b, W_b, and V_b are the set of generators, wind farms, and photovoltaic plants connected to bus b, respectively; $o_1(l) = b$ and $o_2(l) = b$ are the transmission lines where power is injected into and flows out of node b, respectively; $P_{w,t}^0$ and $P_{v,t}^0$ are the amount of dissipation of wind farms w, and photovoltaic plants v, respectively; $P_{l,t}^0$ is the transmission power of line l at period t (positive and negative represent the direction); $L_{b,t}$ is the amount of load at node b at period t; $\Delta P_{\text{L}}^{\text{PDR}}$ is the amount of load change at node b at period t after the execution of the PDR; $\Delta P_{\text{L}}^{0,1\text{IR}}$ is the amount of IDR.

5. Line current, transmission capacity, phase angle constraints

$$\begin{cases} P_{l,t}^0 = \frac{\theta_{o,(l)=t}^0 - \theta_{o2(l)=t}^0}{x_l} \\ -P_l^{\max} \le P_{l,t}^0 \le P_l^{\max} \\ \theta \le \theta \le \bar{\theta} \end{cases} \quad \forall b,l,t \tag{20}$$

where: $\theta_{\text{q}(l)=t}^0$ and $\theta_{o2(l)=t}^0$ are the voltage phase angles of the transmission line l into and out of the bus; x_l is the line l reactance; $P_l^{\max}$ is the upper limit of the transmission capacity of line l; $\bar{\theta}$ and θ are the upper and lower limits of the voltage phase angle $\theta_{b,t}^0$.

6. Unit output constraints

$$\begin{cases} P_{g,t}^{0}+R_{g,t}^{+}\le P_{g}^{\max}i_{g,t} \\ P_{g,t}^{0}-R_{g,t}^{-}\ge P_{g}^{\min}i_{g,t} \end{cases} \quad \forall g,t \tag{21}$$

where: $P_g^{\max}$ and $P_g^{\min}$ are the maximum and minimum output values of thermal power units g, respectively.

7. Unit climbing constraints

$$\begin{cases} \left(P_{g,t}^{0}+R_{g,t}^{+}\right)-\left(P_{g,t-1}^{0}-R_{g,t-1}^{-}\right) \\ \le R_{U,g}\left(1-\mu_{g,t}\right)+P_{g}^{\min}\mu_{g,t} \\ \left(P_{g,t-1}^{0}+R_{g,t-1}^{+}\right)-\left(P_{g,t}^{0}-R_{g,t}^{-}\right) \\ \le R_{D,g}\left(1-v_{g,t}\right)+P_{g}^{\min}v_{g,t} \end{cases} \quad \forall g,t \tag{22}$$

where: $R_{U,g}$ and $R_{D,g}$ are the maximum values of upward and downward climb of the unit, respectively; $\mu_{g,t}$ and $v_{g,t}$ are $0-1$ variables, which are indicated as the start-up and shut-down states of the unit, respectively.

8. Unit reserve capacity constraints

$$\begin{cases} 0\le R_{g,t}^{+}\le R_{g,t,\max}^{+} \\ 0\le R_{g,t}^{-}\le R_{g,t,\max}^{-} \end{cases} \quad \forall g,t \tag{23}$$

$$\begin{cases} \sum_{g\in N_G}R_{g,t}^{+}+\sum P_{\mathrm{L}}^{\mathrm{DRR}}\ge R_{\min}^{+} \\ \sum_{g\in N_G}R_{g,t}^{-}\le R_{\min}^{-} \end{cases} \quad \forall t \tag{24}$$

where: $R_{g,t,\max}^{+}$and $R_{g,t,\max}^{-}$are the upper limit values of upward and downward spare capacity that can be provided by the unit g at the moment t for the transition from the day-ahead phase to the intra-day phase, respectively; $R_{\min}^{+}$and $R_{\min}^{-}$are the minimum values of the total upward and downward spare capacity required by the power system, respectively.

9. Wind farm, photovoltaic plant constraints

$$\begin{cases} 0\le P_{w,t}^{0}\le A_{w,t}^{0} \\ 0\le P_{v,t}^{0}\le A_{v,t}^{0} \end{cases} \tag{25}$$

Where: $A_{v,t}^{0}$ and $A_{v,t}^{0}$ are the predicted values of power available for wind farm w and photovoltaic plant v at the moment t, respectively.

10. PDR, IDR constraints

$$\begin{cases} 0\le\Delta P_{\mathrm{L}}^{\mathrm{IDR}}\le P_{\mathrm{L}}^{\mathrm{IDR}}\le P_{\mathrm{L}}^{\mathrm{IDR,max}} \\ 0\le\Delta P_{\mathrm{L}}^{\mathrm{PDR}}\le P_{\mathrm{L}}^{\mathrm{PDR,max}} \end{cases} \tag{26}$$

where: $P_{\mathrm{L}}^{\mathrm{IDR,max}}$ and $P_{\mathrm{L}}^{\mathrm{PDR,max}}$ are the upper limit values of IDR and PDR loads at the period t, respectively.

3.2. Intraday phase optimization model

1. Objective function

$$\begin{aligned} \max_{U}\min C_{sub}=&\sum_{t=1}^{N_T}\sum_{g=1}^{N_G}\left(C_g^{1,R+}\Delta P_{g,t}^{1+}+C_g^{1,R-}\Delta P_{g,t}^{1-}\right) \\ &+\sum_{b=1}^{N_B}C_{b,t}^{1,\mathrm{IR}}\Delta P_{\mathrm{L}}^{1,\mathrm{DR}} \\ &+C^{w}\sum_{w=1}^{N_w}\left(A_{w,t}^{1}-P_{w,t}^{1}\right) \\ &+C^{v}\sum_{v=1}^{N_v}\left(A_{v,t}^{1}-P_{v,t}^{1}\right) \end{aligned} \tag{27}$$

where: the superscript " 1 " represents the physical quantity of the intraday stage; $C_g^{1,R+}$ and $C_g^{1,R-}$ are the reserve costs of the calling unit up and down in the intraday stage, respectively; $\Delta P_{g,t}^{1+}$ and $\Delta P_{g,t}^{1-}$ are the reserve capacities of the calling unit up and down, respectively; $C_{b,t}^{1,\mathrm{IDR}}$ and $\Delta P_{\mathrm{L}}^{1,\mathrm{IDR}}$ are the costs and capacities of the calling IDR in the intraday stage, respectively; N_w and N_v are the number of wind farms and photovoltaic power stations, respectively; $P_{w,t}^{1}$ and $P_{v,t}^{1}$ are the amount of the consumption of the wind farms w and photovoltaic power stations v in the intraday stage, respectively; C^w and C^v are the penalty costs of abandoning wind and solar power, respectively; $A_{w,t}^{1}$ and $A_{v,t}^{1}$ are the wind and photovoltaic power available in the intraday stage at the time of t, respectively.

2. Power balance constraints

$$\begin{aligned} &\sum_{g\in G_b}P_{g,t}^{1}+\sum_{w\in W_b}P_{w,t}^{1}+\sum_{v\in V_b}P_{v,t}^{1}-L_{b,t}-\Delta P_{\mathrm{L}}^{\mathrm{PDR}}+\Delta P_{\mathrm{L}}^{1,\mathrm{IDR}} \\ &=\sum_{l:0e_2(l)=b}P_{l,t}^{1}-\sum_{l:0_1(l)=b}P_{l,t}^{1} \quad \forall b,t \end{aligned} \tag{28}$$

3. Transmission capacity, phase angle constraints

$$-P_l^{\max}z_l\le P_{l,t}^{1}\le P_l^{\max}z_l \quad \forall l,t \tag{29}$$

$$\underset{\theta}{\theta}\le\theta_{b,t}^{1}\le\bar{\theta} \quad \forall b,t \tag{30}$$

where: z_l is a $0-1$ integer variable to describe transmission line faults, taking 0 to indicate line faults and 1 to indicate normal line operation.

4. Unit reserve constraints

$$\begin{cases} P_{g,t}^{1} & = P_{g,t}^{0} + \Delta P_{g,t}^{1+} - \Delta P_{g,t}^{1-} \\ & 0 \le \Delta P_{g,t}^{1+} \le R_{g,t}^{+} \\ & 0 \le \Delta P_{g,t}^{1-} \le R_{g,t}^{-} \end{cases} \quad \forall g,t \tag{31}$$

5. IDR constraints

$$0 \le \Delta P_{\mathrm{L}}^{1,\mathrm{IDR}} \le P_{\mathrm{L}}^{\mathrm{IDR}} \tag{32}$$

6. Wind and photovoltaic output constraints

$$\begin{cases} 0 \le P_{w,t}^{1} \le A_{v,t}^{1} & \forall w,t \\ 0 \le P_{v,t}^{1} \le A_{v,t}^{1} & \forall v,t \end{cases} \tag{33}$$

3.3. Uncertainty set

Based on the day-ahead-intraday two-stage robust reserve model, the uncertainty set in this paper includes the uncertainty of wind and photovoltaic fluctuation and the uncertainty of transmission line failure and shutdown. Where Π_l denotes the uncertainty limit of the transmission line; $\Pi_{w,t}$ denotes the number of time periods with fluctuations in wind power output, and $\Pi_{v,t}$ denotes the number of time periods with fluctuations in photovoltaic power output. The larger the uncertainty set is, the more worst-case scenarios exist in the model, and the more robust the solved day-ahead-intraday two-phase scheduling strategy is. Since the economy of grid operation is affected by the scheduling strategy, the uncertainty set is adjusted to achieve a balance between the economy and security of the model. The uncertainty set U established in this paper can be expressed by Eqs. (34) to (36):

$$\begin{cases} A_{w,t}^{1} = A_{w,t}^{0} + z_{w,t}^{+}\left(A_{w,t}^{\max} - A_{w,t}^{0}\right) - z_{w,t}^{-}\left(A_{w,t}^{0} - A_{w,t}^{\min}\right) \\ z_{w,t}^{+} + z_{w,t}^{-} \le 1 \\ \sum_{t=1}^{N_t}\left(z_{w,t}^{+} + z_{w,t}^{-}\right) \le \Pi_{w,t} \\ \forall w,t \end{cases} \tag{34}$$

where: $A_{w,t}^{\max}$ and $A_{w,t}^{\min}$ are the upper and lower limit values of the fluctuation of wind farm w in period t, respectively; $z_{w,t}^{+}$and $z_{w,t}^{-}$are $0-1$ integer variables used to indicate whether or not wind farm w fluctuates in period t; $A_{v,t}^{0}$ is the predicted value of wind farm w in period t.

$$\begin{cases} A_{v,t}^{1} = A_{v,t}^{0} + z_{v,t}^{+}\left(A_{v,t}^{\max} - A_{v,t}^{0}\right) - z_{v,t}^{-}\left(A_{v,t}^{0} - A_{v,t}^{\min}\right) \\ z_{v,t}^{+} + z_{v,t}^{-} \le 1 \\ \sum_{t=1}^{N_t}\left(z_{v,t}^{+} + z_{v,t}^{-}\right) \le \Pi_{v,t} \\ \forall v,t \end{cases} \tag{35}$$

where: $A_{v,t}^{\max}$ and $A_{v,t}^{\min}$ are the upper and lower limit values of the fluctuation of photovoltaic plant v in period t, respectively; $z_{v,t}^{+}$and $z_{v,t}^{-}$are $0-1$ integer variables to indicate whether photovoltaic plant v fluctuates in period t; $A_{v,t}^{0}$ is the predicted value of photovoltaic plant v in period t.

$$\sum_{l=1}^{N_L} z_l \le \Pi_l \tag{36}$$

where: N_L denotes the number of transmission lines.

4. Model solution

According to the existing literature, the solution methods for such problems mainly include the affine rule, Benders pairwise cut-plane method, and the column and constraint generation algorithm (C&CG). The affine rule regulates the power fluctuation in the intraday phase according to the allocation coefficients of the thermal power units and transforms the multilayer optimization problem into a single-layer problem to be solved directly. However, the optimization results obtained by using this algorithm are often unsatisfactory. The Benders pairwise cut-plane method is used to solve the problem by decomposing the two-stage robust optimization into a main problem (MP) and subproblem (SP) by means of the Karush-Kuhn-Tucker (KKT) conditions or Strong-Duality-Theory (SDT) to achieve iterative convergence by using the solution results of the subproblems as the constraints added to the master problem.

The C&CG algorithm is similar in principle to the Benders' dyadic cut-plane method, and the core idea is to continuously add the relatively bad scenarios and corresponding subproblem decision variables on the basis of the deterministic optimization solution. The core idea is that on the basis of the deterministic optimization solution, the relatively bad scenarios and the corresponding decision variables and constraints of the subproblems are continuously added, so that the upper and lower bounds of the objective function are continuously improved until the algorithm converges, and this algorithm is also known as the "recourse (recourse)". Since the solution efficiency of the C&CG algorithm is better than that of Benders' dyadic cut-plane method, this paper adopts the C&CG algorithm to solve the two-phase robust reserve problem of day-ahead-intraday, and the specific steps are as follows:

$$\min_{x^0 \in \Omega^0}\left(c^0\right)^{\mathrm{T}} x^0 + \max_{z \in U}\left(b_0^{\mathrm{T}} u_w + b_1^{\mathrm{T}} u_v + \min_{x^1 \in \Omega^1}\left(c^1\right)^{\mathrm{T}} x^1\right) \tag{37}$$

$$\Omega^0 = \left\{x^0 \mid \mathrm{A}x^0 \le a\right\} \tag{38}$$

$$\begin{aligned} U = \{z \mid & u_w = u_w^0 + \Delta U_w^+ z_w^+ + \Delta U_w^- z_w^-, u_v \\ & = u_v^0 + \Delta U_v^+ z_v^+ + \Delta U_v^- z_v^- \\ & B_w \left(z_w^+ + z_w^-\right) \le \Gamma_w, B_v \left(z_v^+ + z_v^-\right) \\ & \le \Gamma_v, B_l z_l \le \Gamma l\} \end{aligned} \tag{39}$$

$$\Omega^1 = \left\{x^1 \mid Dx^1 \le Ex^0 + F_0 u_w^0 + F_1 u_v^0 + Gz + d\right\} \tag{40}$$

where: x^0 is the first stage control variable, including $P_{g,t}^0, R_{g,t}^+, R_{g,t}^-, i_{g,t}, P_{w,t}^0, P_{v,t}^0, P_{l,t}^0, \theta_{b,t}^0, \mu_{g,t}, v_{g,t}$; x^1 is the second-stage control variable, including $\Delta P_{g,t}^{1+}, \Delta P_{g,t}^{1-}, P_{w,t}^1, P_{v,t}^1, \theta_{b,t}^1, P_{l,t}^1$; u_w^0 and u_w represent the amount of wind power available for the first and second phases, respectively; u_v^0 and u_v denote the first and second stage of available photovoltaic power, respectively; $z = \left(z_w^+, z_w^-, z_v^+, z_v^-, z_l\right)$ is a $0-1$ integer variable to represent wind power uncertainty $\left(z_w^+, z_w^-\right)$, photovoltaic uncertainty $\left(z_v^+, z_v^-\right)$and transmission line forced outages (z_l). Eq. (37) is the objective function of the two-stage model; Eq. (38) represents the first-stage constraints, including constraints Eqs. (18-26); Eq. (39) is the uncertainty set, including Eqs. (34-36); and Eq. (40) represents the second-stage constraints, including constraints Eqs. (28-33). c^0, b_0, b_1, c^1, A, $a, \Delta U_w^+, \Delta U_w^-, \Delta U_v^+, \Delta U_v^-, B_w, B_v, B_l, \Gamma_w, \Gamma_v, \Gamma_l, D, E, F, G, d$ are the matrix of constants corresponding to the objective function and constraints.

The master problem, which includes the first stage model as well as the worst operating condition constraints found by the subproblems, is shown in Eqs. (41) and (42) during the i th iteration:

$$\min\left(\left(c^0\right)^{\mathrm{T}} x^0 + \eta\right) \tag{41}$$

$$\text{s.t.} = \begin{cases} \mathrm{A}x^0 \le a \\ \eta \ge b_0^{\mathrm{T}} u_{w,(k)}^* + b_1^{\mathrm{T}} u_{v,(k)}^* + (c^1)^{\mathrm{T}} x_{(k)}^1 \quad 0 \le k \le i-1 \\ Dx_{(k)}^1 \le Ex^0 + F_0 u_w^0 + F_1 u_v^0 + Gz_{(k)}^* + d \quad 0 \le k \le i-1 \end{cases} \tag{42}$$

Where: $u_{w,(k)}^*, u_{v,(k)}^*, z_{(k)}^*$ are the worst-case operating conditions solved by the lower-level problem; $x_{(k)}^1$ is a new optimization variable for the main problem; η is the objective function value of the second stage to be optimized.

The subproblem is a two-layer max-min optimization problem, and the inner minimization problem is transformed into a maximization problem by means of strong dyadic theory, and the model of the transformed subproblem at the first iteration is:

$$\begin{aligned} \max & \left(b_0^{\mathrm{T}} u_w + b_1^{\mathrm{T}} u_v\right. \\ & \left. + \left(Ex_{(i)}^0 + F_0 u_w^0 + F_0 u_v^0 + Gz + d\right)^{\mathrm{T}} \lambda\right) \end{aligned} \tag{43}$$

$$\text{s.t.} = \begin{cases} D^{\mathrm{T}}\lambda \le c^0 \\ \lambda \le 0 \\ z \in U \end{cases} \tag{44}$$

The transformed model contains the bilinear term $z^{\mathrm{T}}\lambda$. Since z is a $0-1$ integer variable, the large M method is applied to introduce the auxiliary variable θ strictly linearized as shown in Eqs. (45) to (48):

$$\theta \ge -M_2 z \tag{45}$$

$$\theta \ge \lambda \tag{46}$$

$$\theta \le \lambda - M_2(z-1) \tag{47}$$

$$\theta \le 0 \tag{48}$$

5. Results and discussion

In this paper, a two-stage robust reserve coordinated operation model based on real-time price is constructed to carry out the day-ahead-intraday optimal dispatch analysis using an improved 6-node system as a regional power grid (including 3 thermal power units and 11 transmission lines). Key values such as upper and lower limits of thermal power unit output power, coal consumption coefficients, and start/stop times are referenced to standard IEEE data. The predicted values and maximum fluctuation ranges of wind farms at each moment are shown in Appendix Figure A4. The forecast value and maximum fluctuation range of the photovoltaic power plant at each moment are shown in Appendix Figure A5. The forecast demand curve of system load at each moment is shown in Appendix Figure A6. The photovoltaic power plant and wind power plant are connected to node 4 and node 5, and the distribution topology of thermal power units is shown in Appendix Figure A7.

5.1. The influence of uncertainty set on system robustness

In order to explore the impact of wind and photovoltaic uncertainty and transmission line failure outage on the robustness of system operation, the analysis of different volatility scenarios of renewable energy sources and the optimization results of four operation scenarios as well as the analysis of total cost of each scenario under its worst operation condition are given in this paper, respectively.

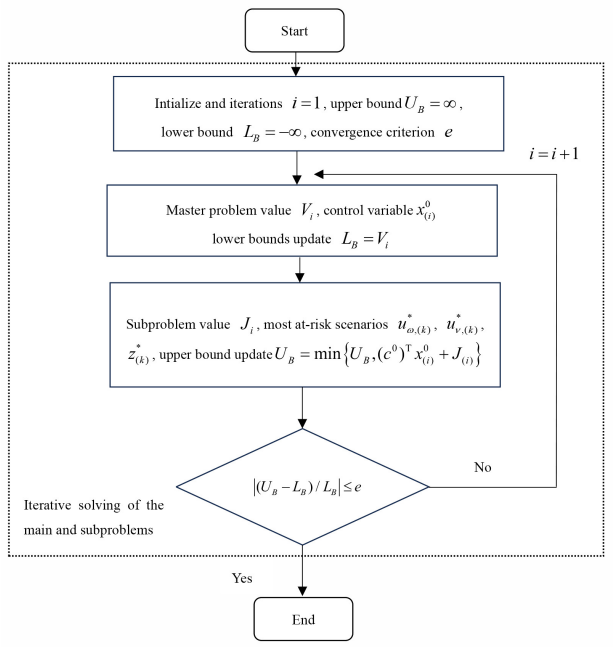

Fig. 1. flow chart

Scenario 1: Deterministic scheduling that does not take into account wind and photovoltaic uncertainties and transmission line failure outages.

Scenario 2: Consider only wind and photovoltaic uncertainties.

Scenario 3: Only transmission line failure outages are considered.

Scenario 4: Consider wind and photovoltaic uncertainty and transmission line failure outages.

Where the worst operating condition is the operating condition that maximizes the total cost of system operation based on the scheduling plan determined for each scenario and the given uncertainty set, which is set to 24,8 , and 1 for Π_w, Π_v, and Π_l, respectively.

Table 1 compares the total scheduling cost and computational time of robust reserve optimization under the effect of different wind and photovoltaic uncertainty sets. From the table, it can be seen that the total scheduling cost and computation time for the worst-case scenario of the robust optimization model gradually increase when the wind- photovoltaic -scenery volatility increases from 4.17% to 41%. The above results show that the higher the number of fluctuation periods, the more complex the wind and photovoltaic output model for the worst-case scenario under consideration is, and therefore the computation time increases. At the same time, the dispatch cost according to the uncertainty set in the intraday phase also increases gradually, implying that the system synergizes the regulation and control tools of thermal unit reserve, IDR, and PDR to optimize the robustness of the grid operation.

As can be seen in Table 2, comparing Scenarios 1 and 2, the system reserve cost increases by \$21,209 after considering the wind and photovoltaic uncertainties, and the intraday phase cost increases from 0 to \$57,594, and increases as the risk of uncertainty becomes greater. Comparing Scenarios 1 and 3, the significant increase in total worst-case cost after considering transmission line failure outages indicates that the system requires more reserve outages to cope with this uncertainty, a result that reflects the necessity of transmission line failure outages. Scenario 4 has the largest set of uncertainties to cope with and therefore requires the highest dispatch costs, with unit reserve and IDR reserve requiring increased outages to maintain system robustness. Taken together, the dispatch scheme considering multiple uncertainty sets increases the total dispatch cost, but the ability to withstand multiple risks is greatly enhanced, validating the effectiveness of the day-ahead-intraday two-stage robust reserve model.

5.2. The influence of uncertainty set on system robustness

In the modeling process, the nonlinear part of the fuel cost function of thermal power units needs to be linearized in segments to improve the computational efficiency of the solver. In order to explore the effectiveness of the segmented model, the number of segments is continuously refined in this paper to compare the performance of various aspects of the robust reserve optimization model, as shown in Table 3 and Fig. 3. At the same time, the power square term of the thermal power unit after the segmentation treatment is further compared with the power square term before the unprocessed treatment to analyze the power difference before and after the segmentation refinement, as shown in Fig. 2.

As can be seen from Table 3 and Fig. 3 , as the number of segments increases, the square term of the thermal power unit is constantly refined, and the error cost is reduced from \$15,270 to \$800, which is gradually leveled off from the original plummeting trend, indicating that the effectiveness of the segment processing model proposed in this paper, but the computation time is also increased. When the number of segments increases the error cost tends to 0, and the complexity of the model so that the calculation time becomes more, this practice is not worth it. It can be seen that the determination of the number of segments must be considered in terms of both error cost and running time, and the model in this paper can further give the optimal number of segments from the scheduling point of view.

Table 1. Optimization results for different scenery volatility scenarios

Renewable energy scenarios	Uncertainty set Π_w	Uncertainty set Π_v	Energy volatility/%	Total dispatch cost/$	Intraday phase cost/$	Computing time/s
1	1	1	4.17	327120	44274	66.68
2	4	4	16.67	329650	46835	66.9
3	8	8	33.33	332660	49707	67.15
4	12	12	50	335520	52569	67.50
5	16	16	66.67	338010	55042	67.89
6	20	20	83.33	339910	56550	82.96
7	24	24	100	341660	57594	89.92

Table 2. Optimization results of different operating scenarios

Scenario	Worst Case Total Dispatch costs / $	Total reserve cost /$ Unit reserve	Total reserve cost /$ IDR reserve	Unit operating cost / $	Intraday phase /$
1	247970	5510	24025	222940	0
2	341660	26719	24025	215820	57594
3	393170	26327	22738	230150	91453
4	398500	25802	27987	229670	97540

Table 3. Optimization results of segmented linearization process

Segmentation ω	Two-stage total cost/$	Unit operating cost/$	Power difference /MW^2	Error cost /$
2	356930	231030	18082	15270
3	347760	221930	9371	6100
4	345450	219600	6446	3790
5	344810	219430	4590	3150
6	344040	218240	3129	2380
7	343300	217470	2547	1640
8	342930	217080	2001	1270
9	342660	216820	1347	1000
10	342460	216620	1177	800

Fig. 2 visualizes the relationship between the number of segments from $\omega = 2$ to $\omega = 5$ and the power error at each time period. As can be seen from the figure, when the number of segments increases, the power error of the model gradually decreases, and the change is especially obvious in the midday period (11:00-14:00). The above results show that refining the nonlinearization function of the thermal power unit can reduce the total cost and power error values of the two phases of the day-ahead-intraday period and improve the robustness of the thermal power unit to the two-phase optimization model.

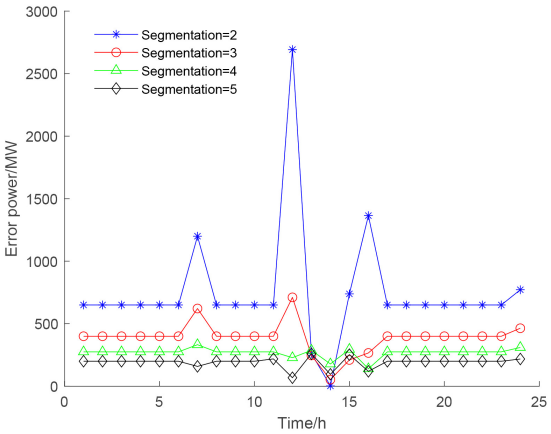

Fig. 2. Error power

5.3. Comparison of solution methods

In order to validate the effectiveness of the day-ahead-intraday two-stage robust reserve optimization model, two solution scenarios are constructed in this paper: (1) the C&CG+SDT scenario adopted in this paper; (2) the C&CG+KKT scenario is adopted. The validation scenario selects scheme II, and the uncertainty sets Π_w and Π_v are not restricted. The optimization results are shown in Table 4 and Fig. 4.

To show the superiority of the proposed method, wind and photovoltaic fluctuations of the two-stage model in finding the worst scenario are given in this paper. As can be seen from Table 4, the unit operating cost and IDR reserve

Table 4. Comparison of optimization results of different solving methods

Method	Two-stage total cost/ $	Unit operating cost/ $	Reserve cost / $		Wind fluctuation range		Photovoltaic fluctuation range		Intra-day stage cost/ $
			Unit	IDR	↑	↓	↑	↓	
KKT	325460	215830	23654	24025	24	0	16	0	44457
SDT	341660	215830	26700	24025	10	14	9	15	57614

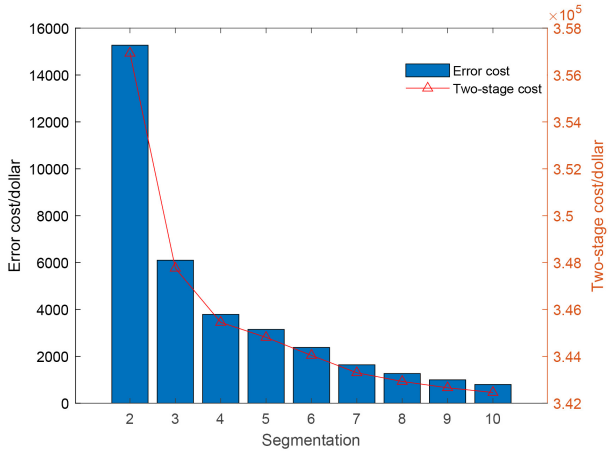

Fig. 3. Piecewise linearization cost

cost of the two methods are the same, and the difference is that the optimization cost of the unit reserve is different. This is because the uncertainty of the scenery predicted by the KKT algorithm exists only in the upper interval, whereas the intraday phase of the worst-case scenario predicted by the SDT algorithm is more expensive to adjust to cope with the new energy output that fluctuates more irregularly. The total cost of the model developed in this paper is $16,200 higher than that of the KKT model, indicating that the proposed strategy can predict the worse operating conditions to adjust the reserve unit output to enhance the robustness of the operating system, further validating the effectiveness of the methodology in this paper.

5.4. DR analysis under the real-time price mechanism

To verify the effectiveness of the load response model under the real-time price mechanism based on load classification, the load response curve under the real-time price mechanism is shown in Fig. 5, and this paper set the proportion of the three types of loads to be 60%, 20%, and 20%, respectively, as shown in Fig. 6. This paper set the uncertainty set $\Pi_w = 8, \Pi_v = 8$.

To further illustrate the impact of incentivized demand response on the robustness of the grid operation, Table 5 gives the comparison of the system under worst-case conditions as the upper limit of the participating incentivized demand response loads changes. From the table, it can be seen that as the participating IDR load keeps increasing, the IDR reserve cost becomes larger, replacing the unit output to reduce the total cost under the worst case. It shows that the incentive-based demand response is more effective in enhancing the robustness of the grid and reducing the risk of scenic uncertainty by directly controlling the load to enhance the system reserve capacity.

6. Conclusion

This paper presents a two-stage robust standby optimization considering real-time tariff day-ahead intraday. The two demand-side response means, price-based and incentive-based, are optimized synergistically, while the system integrates the uncertainty of wind power and transmission line failure outages. The following conclusions can be obtained from the calculation example:

1. The load classification-based demand response model proposed in this paper is closer to the actual situation, which can more accurately construct the day-ahead-intraday two-phase robust reserve optimization model, giving full play to the flexibility of the two kinds of demand response, and then improve the overall operating efficiency of the system. The robustness of the reserve optimization operation system can be improved by comprehensively considering the uncertainty of scenery output and transmission line failure outage. At the same time, the balance between the economy and the robustness of the system operation can be realized by adjusting the size of the uncertainty set.

2. Due to the different research focuses of the articles, this paper has not yet considered the impact of real-time price uncertainty, which is an important factor in system operation, and the probabilistic information of the uncertainty factors will be further explored to be added into the robust optimization model in the future research work.

3. Considering the demand and allocation of reserve capacity in real-time price is an important issue in elec-

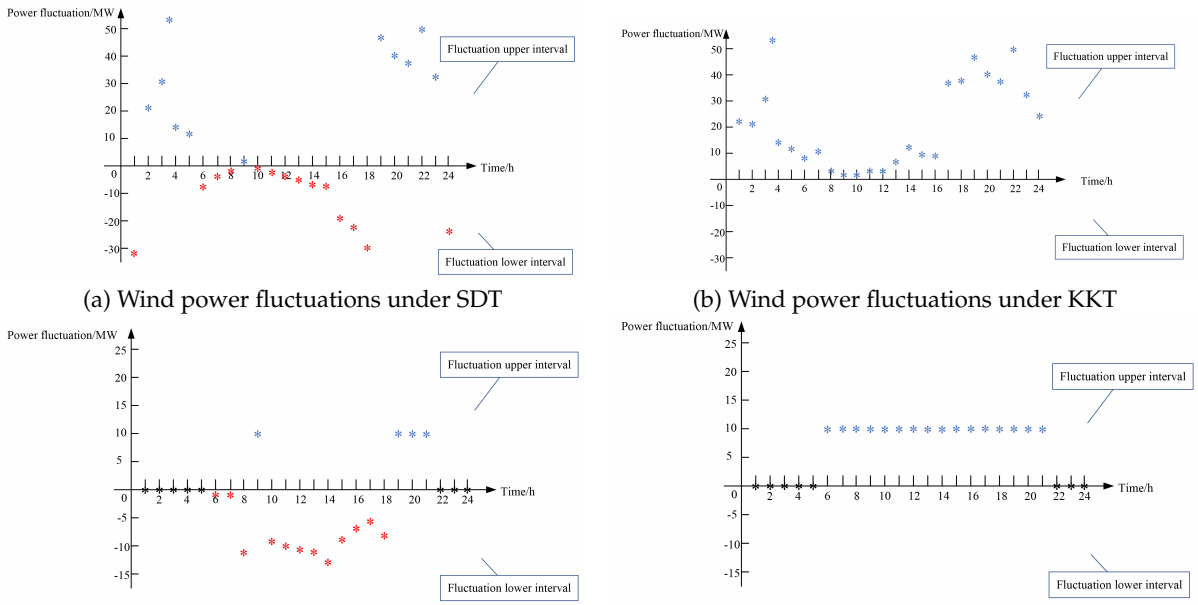

(a) Wind power fluctuations under SDT

(b) Wind power fluctuations under KKT

(c) photovoltaic fluctuations under SDT

(b) (d) photovoltaic fluctuations under KKT

Fig. 4. New energy volatility uncertainty

Table 5. Effect of IDR load upper limit on system robustness

IDR load upper limit	Total cost of the worst operating conditions /$	Unit cost /$	IDR reserve cost /$	Intra-day stage cost /$
0	345190	288170	7624	31888
0.1	319950	243290	12819	39070
0.2	304000	211960	17860	44189
0.3	293480	189220	21275	48865
0.4	287300	172840	20677	56277

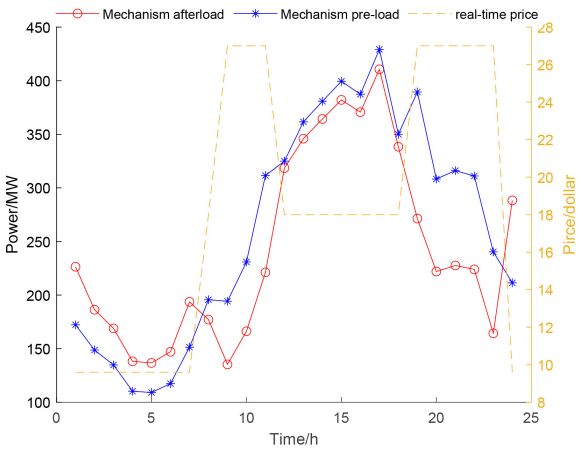

Fig. 5. Load response curve

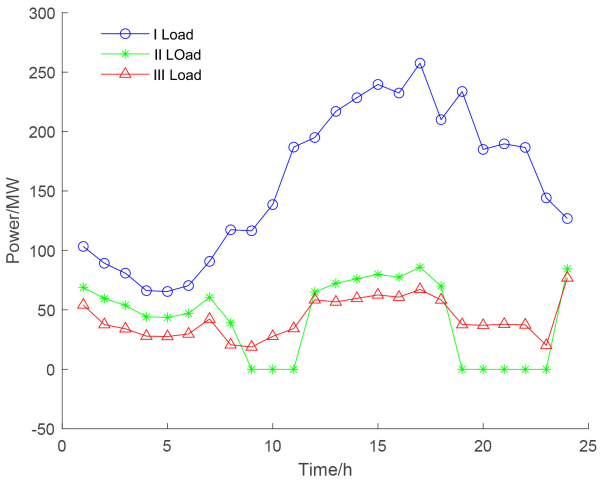

Fig. 6. Load classification

tricity market design. The research in this paper can help provide some implications for the development of market mechanisms and rules.

Acknowledgements

This research was financially supported by Fujian Natural Science Foundation Project under the grant 2022J01948, and Scientific Research Development Foundation of Fujian University of Technology under the grant GY-Z17149.

References

[1] P. Ju, T. Jiang, and H. Huang, (2023) *"Brief discussion on the "three-self" nature of the new power system"* **Proc. CSEE *43***: 2598–2607. DOI: 10.13334/j.0258-8013.pcsee.223257.

[2] C. Zhang, L. Liu, H. Cheng, J. Lu, J. Zhang, and G. Li, (2022) *"Review and prospects of planning and operation optimization for electrical power systems considering frequency security"* **Power System Technology *46***(1): DOI: 10.13335/j.1000-3673.pst.2021.0844.

[3] L. Yang, S. Zhang, H. Cheng, and J. Lv, (2022) *"Regional low-carbon integrated energy system planning: key technologies and challenges"* **Power System Technology *46***(09): 3290–3304. DOI: 10.13335/j.1000-3673.pst.2022.1522.

[4] B. Hu and L. Wu, (2015) *"Robust SCUC considering continuous/discrete uncertainties and quick-start units: A two-stage robust optimization with mixed-integer recourse"* **IEEE Transactions on Power Systems *31***(2): 1407–1419. DOI: 10.1109/TPWRS.2015.2418158.

[5] Z. Cao, H. Chen, P. Hu, and L. Chen, (2021) *"Day-ahead and intraday two-stage optimal dispatch model of a thermal power plant with energy storage and taking into account the profit"* **Power System Protection and Control *49***: 106–113. DOI: 10.19783/j.cnki.pspc.200957.

[6] Z. Zhenyu et al., (2020) *"Reserve of power system considering renewable-Energy based on risk control"* **Power System Technology *44***(09): 3375–3382. DOI: 10.13335/j.1000-3673.pst.2020.0486.

[7] P. Li, D. Yu, M. Yang, and J. Wang, (2018) *"Flexible look-ahead dispatch realized by robust optimization considering CVaR of wind power"* **IEEE Transactions on Power Systems *33***(5): 5330–5340. DOI: 10.1109/TPWRS.2018.2809431.

[8] Y. Lin, Y. Ding, Y. Song, and C. Guo, (2017) *"A multi-state model for exploiting the reserve capability of wind power"* **IEEE Transactions on Power Systems *33***(3): 3358–3372. DOI: 10.1109/TPWRS.2017.2775188.

[9] C. Luo, Y. Li, H. Xu, L. Li, T. Hou, and S. Miao, (2017) *"Influence of demand response uncertainty on day-ahead optimization dispatching"* **Automation of Electric Power Systems *41***(5): 22–29. DOI: 10.7500/AEPS20160702006.

[10] Y. Zhang, Y. He, M. Yan, C. Guo, S. Ma, and D. Song, (2018) *"Optimal dispatch of integrated electricity-natural gas system considering demand response and dynamic natural gas flow"* **Automation of Electric Power Systems *42***: 1–8. DOI: 10.7500/AEPS20180128005.

[11] B. Zhou, T. Huang, and Y. Zhang, (2017) *"Reliability analysis on microgrid considering incentive demand response"* **Autom. Electr. Power Syst *41***: 70–78. DOI: 10.7500/AEPS20160926016.

[12] J. Yang, Z. Wu, and H. Fang, (2023) *"Collaborative scheduling strategy for renewable energy systems with energy storage based on real time price"* **Energy Storage Technology *51***: 46–53.

[13] Y. Xia, Q. Xu, J. Zhao, and X. Yuan, (2020) *"Two-stage robust optimisation of user-side cloud energy storage configuration considering load fluctuation and energy storage loss"* **IET Generation, Transmission & Distribution *14***(16): 3278–3287. DOI: 10.1049/iet-gtd.2019.1832.

[14] C. Wang, X. Zhang, Y. Xia, H. Xiong, C. Guo, L. Wang, and Y. Wang, (2023) *"A two-stage robust optimal configuration model of generation-side cloud energy storage system based on cooperative game"* **IET Generation, Transmission & Distribution *17***(8): 1723–1733. DOI: 10.1049/gtd2.12473.

[15] Z. Shao, Y. Lin, F. Chen, Y. Zheng, Y. Guo, and X. Yan, *"Distributionally robust low-carbon economic dispatch of electricity-gas-heat integrated energy system considering carbon-green certificate coupling mechanism"* **Electric Power Automation Equipment**: 1–19. DOI: 10.16081/j.epae.202311006.

[16] M. Dong, M. Zhu, C. Xu, and S. Dong, *"Centralized-distributed integrated demand response mechanism for regional integrated energy system considering multiple agents"* **Power System Technology**: 1–16. DOI: 10.13335/j.1000-3673.pst.2023.1345.

[17] F. Chen, X. Zheng, Z. Shao, Y. Guo, Y. Lin, and M. Cai, *"Online calculation of affine arithmetic-based optimal power-gas flow for tracking real-time changes in source and load"* **Power System Technology**: 1–16. DOI: 10.13335/j.1000-3673.pst.2023.1550.

[18] E. Jiang, Z. Chen, L. Shi, J. Hui, S. Lin, and Y. Mi, (2023) *"Cooperative operation strategy of multi-microgrids based on multiple uncertainties and comprehensive contribution rate"* **ACTA ENERGIAE SOLARIS SINICA *44***: 80–89. DOI: 10.19912/j.0254-0096.tynxb.2022-1070.

[19] Y. Li, H. Ye, Y. Cao, Z. Li, and X. Shi, *"High-risk links identification for cascading failures based on the power flow transfer similarity"* **Proceedings of the CSEE**: 1–12. DOI: https://link.cnki.net/urlid/11.2107.TM.20230919.1451.013.

[20] Y. Guo, S. Liu, w. Gao, d. Li, A. Zhang, and X. Jiang, (2024) *"Research on the construction method of cascading outage fault set based on weighted power flow entropy and coupling branch intermediate index"* **Proceedings of the CSU-EPSA *36***: 113–119. DOI: 10.19635/j.cnki.csu-epsa.001299.

[21] L. Yang, J. Wang, X. Li, and H. Liu, (2024) *"A bi-level transmission expansion planning model considering planning-operation coordination of line load rate indices"* **Power System Technology *48***: 1846–1854. DOI: 10.13335/j.1000-3673.pst.2023.0678.